Icarus 302 (2018) 308–318

Contents lists available at ScienceDirect

Icarus

journal homepage: www.elsevier.com/locate/icarus

A reanalysis of ozone on Mars from assimilation of SPICAM observations

James A. Holmes[a,*], Stephen R. Lewis[a], Manish R. Patel[a,b], Franck Lefèvre[c]

[a] School of Physical Sciences, The Open University, Walton Hall, Milton Keynes MK7 6AA, UK
[b] Space Science and Technology Department, Science and Technology Facilities Council, Rutherford Appleton Laboratory, Harwell Campus, Didcot, Oxfordshire OX11 0QX, UK
[c] LATMOS, CNRS/Université Pierre et Marie Curie/UVSQ, Paris France

ARTICLE INFO

Article history:
Received 13 April 2017
Revised 4 October 2017
Accepted 21 November 2017
Available online 22 November 2017

Keywords:
Mars atmosphere
Mars data assimilation
Atmospheres
chemistry

ABSTRACT

We have assimilated for the first time SPICAM retrievals of total ozone into a Martian global circulation model to provide a global reanalysis of the ozone cycle. Disagreement in total ozone between model prediction and assimilation is observed between 45°S–10°S from L_S =135–180° and at northern polar (60°N–90°N) latitudes during northern fall (L_S =150–195°). Large percentage differences in total ozone at northern fall polar latitudes identified through the assimilation process are linked with excessive northward transport of water vapour west of Tharsis and over Arabia Terra. Modelling biases in water vapour can also explain the underestimation of total ozone between 45°S–10°S from L_S =135–180°. Heterogeneous uptake of odd hydrogen radicals are unable to explain the outstanding underestimation of northern polar total ozone in late northern fall.

Assimilation of total ozone retrievals results in alterations of the modelled spatial distribution of ozone in the southern polar winter high altitude ozone layer. This illustrates the potential use of assimilation methods in constraining total ozone where SPICAM cannot observe, in a region where total ozone is especially important for potential investigations of the polar dynamics.

1. Introduction

Observations and modelling of ozone have the potential to greatly improve our understanding of the Martian atmosphere. It can be observed by the strong and wide absorption band centred at 255 nm detectable by UV spectrometers (Perrier et al., 2006) and imagers (Clancy et al., 2016), 9.7 µm at which IR spectrometers can ascertain measurements (Fast et al., 2006) and also indirectly in the 1.27 µm $O_2(a^1\Delta_g)$ emission band (Fedorova et al., 2006; Altieri et al., 2009).

There are a multitude of atmospheric processes which can be investigated by studying the ozone cycle. Firstly, it can be used as a tracer for OH (produced from the photolysis of water vapour), an odd hydrogen radical which readily destroys ozone. The infrared emission of OH has recently been detected by Clancy et al. (2013) and is known to play a key role in the stability of the atmosphere. Ozone has also been found to be quasi-passive in the polar night (Lefèvre et al., 2004) due primarily to the suppression of photochemical ozone destruction and a negligible presence of HO_x (H, OH and HO_2) radicals at this time of the year. The dynamics associated with the northern polar vortex can therefore be traced by monitoring ozone abundance (Holmes et al., 2017), an application raised when investigating recent observations of total ozone (Clancy et al., 2016). Further analysis of the ozone cycle can also provide a broader understanding of the Martian atmospheric chemistry.

Providing a consistent temporal and spatial agreement between models and observations of ozone is also of great benefit in furthering the understanding of important photochemical processes in the Martian atmosphere. Seasonal variations have been known from the first observations of ozone by Mariner 9 (Barth et al., 1973), and more recently been shown to be governed primarily by the hygropause level at different times of the year (Clancy and Nair, 1996). A one-dimensional photochemical model developed by Krasnopolsky (2006, 2009) investigated latitudinal and diurnal variations of photochemical species including ozone. The model does however use a fixed temperature profile and due to its nature is unable to represent horizontal transport. Moreau et al. (1991) used a two-dimensional model to describe vertical profiles of ozone, but this was in a dust-free atmosphere

* Corresponding author.
E-mail address: james.holmes@open.ac.uk (J.A. Holmes).

https://doi.org/10.1016/j.icarus.2017.11.026

and also neglected cloud effects. To investigate the combined dynamical, physical and chemical processes affecting ozone distribution requires ideally a three-dimensional model.

Lefèvre et al. (2004) was the first to use a three-dimensional Martian global circulation model (GCM) coupled to a photochemical module to increase knowledge of the properties of ozone in the Martian atmosphere. The agreement between the model and observations was later improved by inclusion of heterogeneous reactions on HO_x species (Lefèvre et al., 2008) which had previously been theorised (Krasnopolsky and Parshev, 1979), although this has recently been put into question by Clancy et al. (2016) with little evidence of a correlation between total ozone and water ice optical depth retrievals from the Mars Color Imager (MARCI) on the Mars Reconnaissance Orbiter (MRO) spacecraft. Comparisons to spatially averaged observations provide good constraints on the seasonal distribution. For an in-depth approach, identifying differences between models and observations on a range of temporal and spatial scales can identify specific regions where the largest differences exist, and thus a deficiency in our understanding of the physical processes at work. The added spatial dimension hence informs models about the cause and evolution of the differences on a local, rather than global, scale. Higher resolution models with less restricted physical parameterisations can subsequently be used to study the identified area in more depth (Spiga and Forget, 2009), which would otherwise be computationally expensive.

To make optimal use of information, observations and GCMs are combined by the process of data assimilation. The satellites currently orbiting Mars, combined with the future planned satellite missions, create a great opportunity for the development of a data assimilation technique for ozone and more generally trace gases on Mars. Although data assimilation is now commonplace on Earth, it is a fairly new concept for other planetary systems. Data assimilation is becoming an increasingly reliable technique for the input of observations into a GCM to study a variety of topics (Lewis and Barker, 2005; Lewis et al., 2007; Montabone et al., 2006; Hoffman et al., 2012; Greybush et al., 2012; Navarro et al., 2014a; Steele et al., 2014a,b). The majority of these publications use retrievals from the Thermal Emission Spectrometer (TES) aboard the Mars Global Surveyor due primarily to the wealth, and good spatial coverage, of these observations (Conrath et al., 2000). Mars Express carries the Spectroscopy for the Investigation of the Characteristics of the Atmosphere of Mars (SPICAM) instrument from which total ozone can be retrieved (Perrier et al., 2006). Ozone has never before been assimilated for Mars, but is a widespread technique for Earth (Levelt et al., 1996; Eskes et al., 2003; Grassi et al., 2004; Kiesewetter et al., 2010). The SPICAM instrument was the first to provide a spatial and temporal coverage of the global climatology of ozone suitable for data assimilation techniques.

Data assimilation has multiple benefits over direct comparison between GCM simulated and observed quantities; providing estimates for parameters which are not directly observed, additional information on observations from the physical constraints imposed by GCMs, and combining observational datasets to optimise the value of the resulting data set. Assimilating observations of multiple trace gases on Mars in the future will also be achievable, allowing for investigations into interactions between chemical species which will improve our understanding of the martian chemical environment. Chemical rate coefficients defined through reconciling observed and modelled quantities would add to existing determinations of these rate coefficients, which in some cases are poorly constrained by laboratory measurements. The assimilation of total ozone can also be used to inform future investigations on the best observing strategy for upcoming missions such as the ExoMars Trace Gas Orbiter (TGO) and provide a comprehensive analysis, constrained by satellite observations, of the ozone cycle on Mars.

In this paper we investigate the effect of total ozone assimilation using SPICAM data on improving our understanding of the ozone cycle. Section 2 details the GCM and assimilation scheme used in this investigation and Section 3 outlines the SPICAM retrievals and quality control performed on the data. Section 4 provides the results of total ozone assimilation, and Section 5 states the conclusions of this investigation.

2. Global circulation model and assimilation method

To perform the model simulations, we use the UK version of the Laboratoire de Météorologie Dynamique (LMD) Mars GCM (hereafter MGCM). This 4D-model uses the physical parameterisations (Forget et al., 1999) and LMD photochemical module (Lefèvre et al., 2004) shared with a recent version of the LMD Mars GCM coupled to a UK-only spectral dynamical core and semi-Lagrangian advection scheme (Newman et al., 2002). It has been developed in a collaboration between the Laboratoire de Météorologie Dynamique, the Open University, the University of Oxford and the Instituto de Astrofisica de Andalucia. The dust distribution has been prescribed horizontally based on an interpolation of numerous sets of observations from orbiters and landers using a kriging method (Montabone et al., 2015), with a'semi-interactive' two-moment scheme used to freely transport dust vertically in the model (Madeleine et al., 2011). The model was run at T31 resolution in the horizontal, corresponding to a resolution of 5° latitude by 5° longitude, with 32 vertical levels in the range 0–105 km. Vertical levels are much closer to one another near the surface and further spread higher in the atmosphere.

The MGCM includes the latest sub-models to provide the most realistic modelling of the planetary boundary layer and water and dust cycles. A thermal plume model is used to better represent turbulent structures in the planetary boundary layer (Colaïtis et al., 2013). Regarding the martian water cycle, the most recent cloud microphysics package is included (Navarro et al., 2014b) which also accounts for the effects of radiatively active water ice clouds and supersaturation. The photochemical module provides multiple photolytic and chemical reactions with up-to-date reaction rates between 16 advected species including carbon dioxide, water vapour and ozone. It also includes heterogeneous processes removing odd hydrogen radicals, a process which has been shown to improve the agreement between models and observations (Lefèvre et al., 2008). Time-varying dust amounts are also taken into account in the photolytic reactions. Tracers are advected using the semi-Lagrangian advection scheme.

Full details on the production and loss of ozone calculated at each timestep are in Lefèvre et al. (2004). The photolysis rate coefficient is calculated by the Tropospheric Ultraviolet and Visible model adapted to Martian conditions and stored in a lookup table offline to save computational expense. During the day, ozone is considered to be in photochemical equilibrium and implicitly solved as part of the O_x (O and O_3) family. At night, ozone is integrated separately from O with production and loss calculated via the associated chemical reaction rates. The simulations in this investigation are run over the time period of available SPICAM retrievals, which covers the time period from L_S = 341° MY 26 to L_S = 69° MY 28.

The assimilation is performed using a form of the Analysis Correction (AC) scheme (Lorenc et al., 1991) converted to martian conditions, and has been shown in the past to be a computationally inexpensive and robust method (Lewis et al., 2007). Using this methodology, observations of short-lived (and long-lived) species can be supplemented by knowledge of the transport and atmospheric chemistry from a GCM. Other assimilation schemes are also now available for use, including a Local Ensemble Transform Kalman Filter (Navarro et al., 2014a). This particular assimilation

method has however so far not been used to assimilate chemical species.

The method used to assimilate the SPICAM ozone retrievals is largely similar to the method used by Steele et al. (2014b) in assimilating water vapour column retrievals from the TES instrument on the Mars Global Surveyor spacecraft. The observations assimilated into the MGCM are total column ozone retrieved from a nadir-viewing spectrometer in the unit of μm-atm. Chemical tracers in the MGCM are transported and stored as a mass mixing ratio. To compare like for like, the ozone mass mixing ratio q_{im} at each model grid point i and layer m is converted into total ozone D_i in μm-atm using

$$D_i = \frac{X_D}{g} \sum_m q_{im} \mathrm{d}p_{im} \tag{1}$$

where $g = 3.72$ m s^{-2} is the mean acceleration due to gravity on Mars, $\mathrm{d}p_{im}$ is the pressure difference between adjacent model sigma levels, and X_D is the factor to convert total ozone from kg m^{-2} to μm-atm.

The total ozone value from the model is interpolated to the observation location k and the increment to the observed value is calculated as

$$\Delta D_k = D_k^{\mathrm{obs}} - D_k^{\mathrm{model}} \tag{2}$$

where D_k^{model} represents the interpolated model value for observation k. The total ozone increment D_i for a particular model grid point is then calculated using the subset of observations j within a specified radius of influence (equivalent to 540 km at the start of the time window and 340 km at the exact time of the observation) as

$$\Delta D_i = \lambda \sum_j \mu_{ij} \tau_j^2 \widetilde{\mathbf{Q}}_j \Delta D_j, \tag{3}$$

where μ_{ij} is the correlation function (dependent on the horizontal distance r_{ij} between the model grid point i and the observation j currently being analysed), λ is a relaxation coefficient determining the fraction of the analysed increment that is added onto the model field, τ_j^2 is an additional empirical temporal coefficient and $\widetilde{\mathbf{Q}}$ is a normalisation factor which takes into account the ratio of observation to first guess model error and the data density of the observations (Lorenc et al., 1991). Only the model grid points affected by retrievals for a particular iteration of the model are updated by maintaining a separate assimilated total ozone field from the modelled total ozone field. Every 30 minutes (equivalent to one physics timestep of the MGCM), the assimilated total ozone field is compared to the previous assimilated total ozone field from 30 minutes ago in the simulation. Where they differ is where more recent retrievals have updated the field and it is these grid points that are then updated in the modelled total ozone field. After the modelled total ozone has been adjusted due to the increment ΔD_i, this increment needs to be translated back to the modelled ozone mass mixing ratio in preparation for the next dynamical and physical timestep. This is performed using a correction factor C_i for the ozone mass mixing ratio at each model level m, which is a height independent factor and therefore uses the simulated vertical profile of ozone as the best guess. The unconstrained vertical profile of water vapour, as a result of its links to ozone destruction, is a potential source for total ozone differences identified using this scaling method, but this is beyond the scope of the current study. The validity of an independent height factor will be explored in the future through comparison with retrievals of the vertical profile of ozone and water vapour from the NOMAD (Nadir and Occultation for MArs Discovery) instrument (Neefs et al., 2015; Patel et al., 2017). The ozone mass mixing ratio q_{im}^{assim} after assimilation is thus updated by

$$q_{im}^{\mathrm{assim}} = C_i q_{im}^{\mathrm{model}}, \quad \textit{where} \quad C_i = \frac{D_i + \Delta D_i}{D_i} \tag{4}$$

only at grid points i affected by retrievals on the current physics timestep.

Experiments to decide on the best insertion parameters for the data have previously been conducted (Holmes, 2015). For dust opacity and temperature assimilation, a 6 hour time window (5 hours ahead of the observation, and 1 hour after) were used with a reasonably large radius of influence since the fields are relatively slow to vary in time (Lewis et al., 2007). The short lifetime of ozone in sunlit regions suggests a smaller time window to be more appropriate. A 5 hour time window (4 hours before and 1 hour after) was found to be optimal by comparing the average root mean square error (RMSE) of total ozone for several times of year and using different time windows (Holmes, 2015), although the RMSE values varied little for a 4 or 5 hour time window. A 5 hour time window was further decided upon by looking at the diurnal cycle of the total ozone calculated by the MGCM at different times of year where retrievals of total ozone from SPICAM are available, as shown in Fig. 1. By using a larger time window than 5 hours, the risk of smoothing out the rapid decrease of total ozone in the morning is reduced. The local time of the SPICAM total ozone retrievals was also taken into account. Over-mixing and excessive transport of total ozone across the day-night terminator also need to be taken into consideration, issues recognised when assimilating ozone for Earth (Lahoz et al., 2005). To account for possible over-mixing of ozone, the radius of influence for each SPICAM retrieval is decreased (when compared to the assimilation of temperature or dust opacity) since ozone has larger spatial variations over a smaller region than temperature or dust. With a smaller radius of influence, the likelihood that retrievals associated with a high solar zenith angle (only SPICAM retrievals with a solar zenith angle less than 85° were used for the assimilation) could influence the isolated regions of constant darkness during northern and southern winter is also reduced. Most of the SPICAM retrievals have a local time of around 12 p.m. and Fig. 1 indicates that the time window used for the assimilation procedure should also avoid the large differences in total ozone seen at the day-night terminator.

3. Data description

The retrievals assimilated in this study (displayed in Fig. 2a) are from the SPICAM instrument on Mars Express presented in Perrier et al. (2006). The gaps in data from L_S = 70–90° and L_S = 200–240° in Mars Year (MY) 27 result from a night side pericentre preventing observations and other instruments aboard the spacecraft taking priority, respectively. Maximum total ozone values are seen around northern hemisphere spring equinox at northern polar latitudes, as a result of polar night conditions in the recent past and a lack of odd hydrogen species. The SPICAM instrument is able to observe large ozone abundance before water vapour and associated odd hydrogen species are transported into the northern polar regions resulting in destruction of ozone.

The retrieval of total ozone from the Hartley band of absorption (220-280 nm) is described fully in Perrier et al. (2006), and briefly detailed in this section. The outcome of the retrieval process is just over 27,000 high signal-to-noise ratio retrievals for almost one and a half Martian years (L_S = 341° in MY 26 to L_S = 69° in MY 28). The ground resolution at pericentre is around 4 km^2, with an average uncertainty in total ozone of 10–15%. Most, if not all, of the attempts to assimilate ozone on Earth have included archived wind

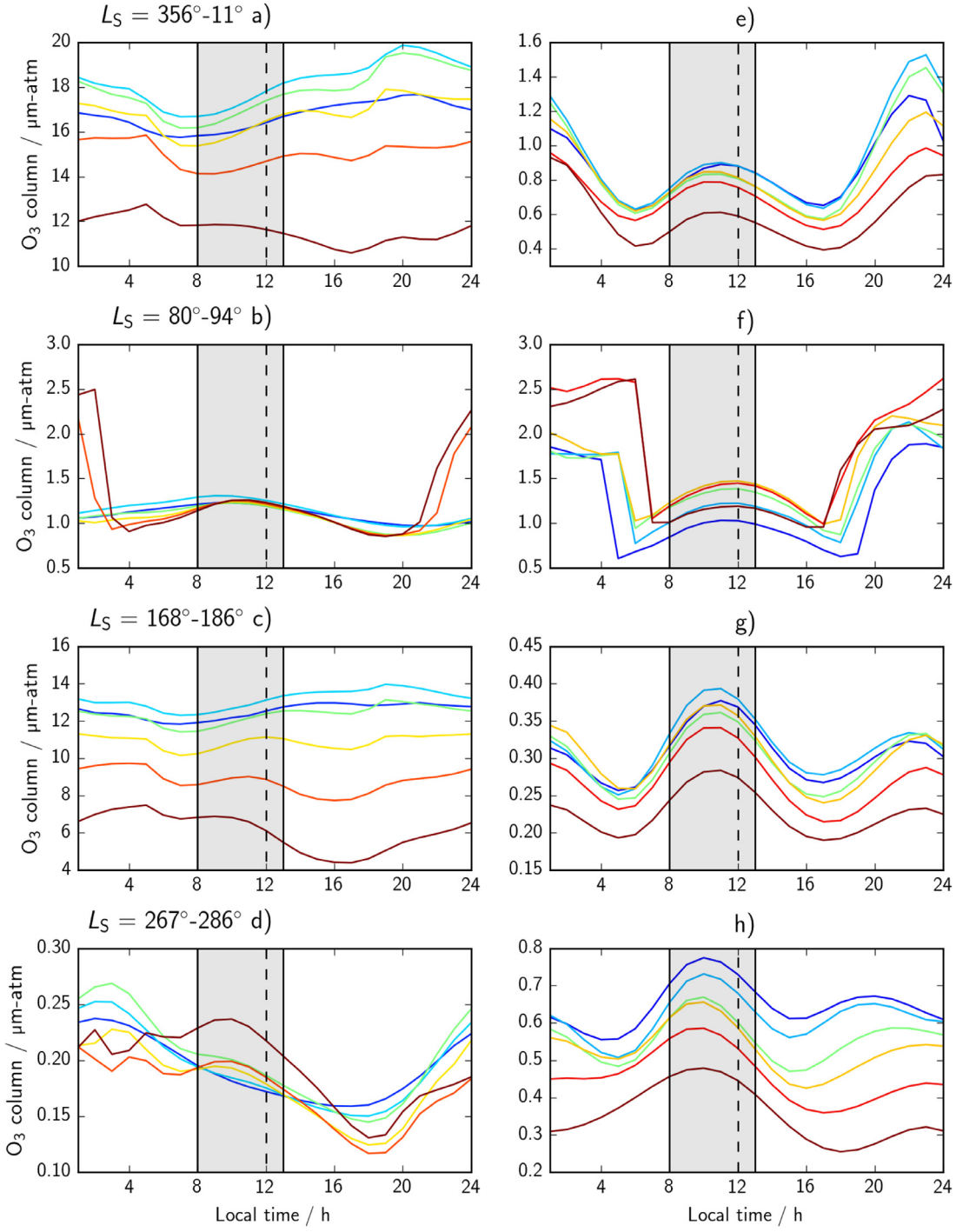

Fig. 1. The diurnal cycle of total ozone for the equinox and solstice periods in the MGCM. Each row corresponds to a different time of the Mars year. a) – c) display northern latitudes from 52.5°N (red) - 77.5°N (blue) in 5° latitudinal increments. d) displays southern latitudes from 52.5°S (red) - 77.5°S (blue). e) – h) display mid-latitudes from 22.5°S (red) - 27.5°N (blue). The shading represents the time window for a retrieval at 12 p.m. Note the different scales for total ozone in each plot. (For interpretation of the references to colour in this figure legend, the reader is referred to the web version of this article.)

data to transport the assimilated species to provide a more robust analysed field. For the first assimilation of ozone for Mars, the dynamically determined wind field from the MGCM is used to transport ozone and all other chemical species, but future investigations could potentially also assimilate thermal profiles alongside ozone retrievals. This highlights another benefit of data assimilation, in that data sparse regions are potentially influenced by SPICAM retrievals of total ozone being advected into the local unobserved region.

Before the SPICAM retrievals are assimilated into the MGCM, they are subject to quality control measures. For the ~27,000 retrievals from SPICAM available, the relative sparseness of the data is an issue for a comprehensive buddy check algorithm, since there are not enough data points to be statistically significant over a sensible spatio-temporal region. A single spurious retrieval can have a large effect on the mean and standard deviation if there are only a handful of observations in the sub sample. Choosing a wide enough margin to get a statistically significant number of

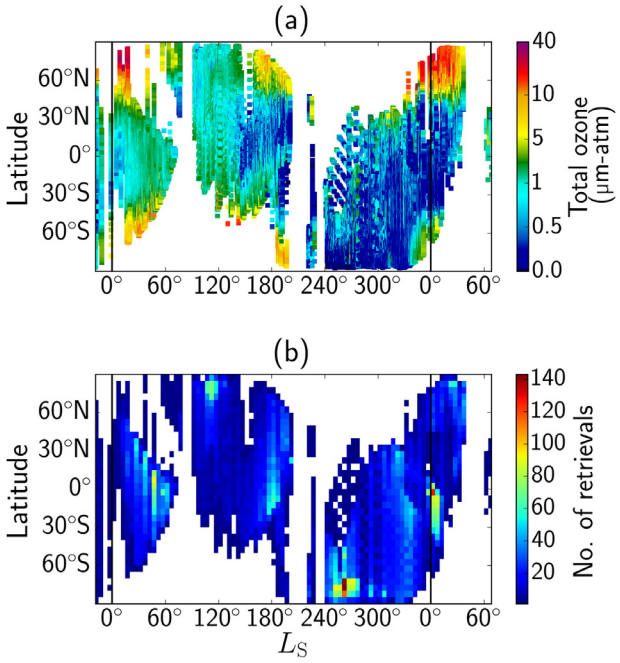

Fig. 2. SPICAM nadir retrievals for $L_S = 341°$ MY 26 to $L_S = 69°$ MY 28 as a function of latitude and solar longitude displaying a) the total ozone abundance and b) number of retrievals. The number of SPICAM retrievals are binned every 5°L_S and 5° latitude.

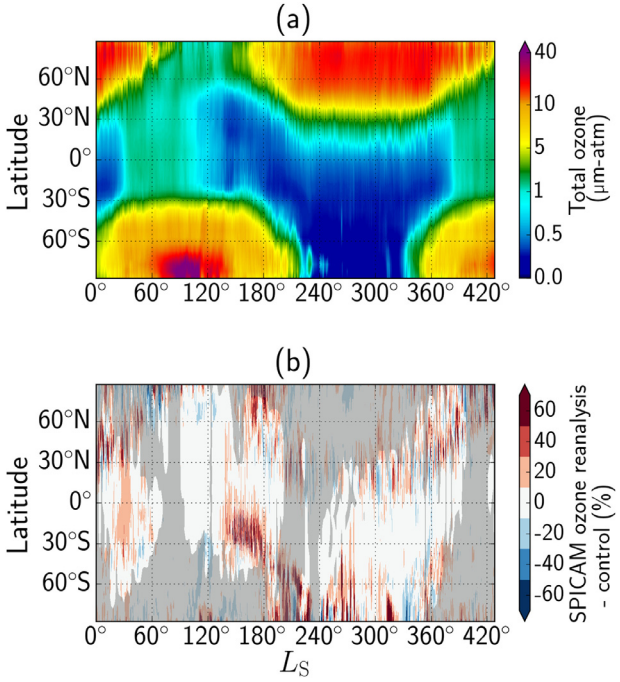

Fig. 3. Assimilated zonally averaged ozone column at 12 p.m. everywhere (top) and the percentage difference (SPICAM ozone reanalysis - control) between the SPICAM ozone reanalysis and control simulation (bottom) for MY 27 and start of MY 28. Shading indicates regions where there are no nearby SPICAM retrievals at the corresponding time and space.

observations would require using observations from multiple days or over large degrees of latitude which would remove any natural variations in the retrievals. Each SPICAM retrieval R_k is instead compared to the retrieval $R_{k\pm1}$ either side of it in time. Spurious retrievals are then flagged up using three criteria; $|R_k - R_{k\pm1}| > 10$ μm-atm, $|L_k - L_{k\pm1}| < 5°$ and $|S_k - S_{k\pm1}| < 1$ where L_k and S_k are the latitude and sol of observation k respectively. A value of 10 μm-atm was chosen to avoid rejection of retrievals which are realistic due to the sharp gradient on the boundaries of the high polar ozone abundance. Only 7 retrievals are found using this method, including retrievals of 38.97, 39.46 and 50.14 μm-atm at high southern latitudes in southern summer. These values are impossible since this region is in almost persistent daylight in southern summer and photolytic and chemical reactions with HO_x species, enhanced due to the sublimation of water vapour from the southern polar cap, prevent the total ozone from reaching anywhere near this level of ozone abundance.

4. Results

To investigate the effect of total ozone assimilation on the seasonal cycle, we ran a 'control' simulation with no assimilation and a second simulation in which total ozone retrievals from SPICAM were assimilated (hereafter the SPICAM ozone reanalysis). Both runs start from the same initial distribution at $L_S = 330°$ in MY 26 with a well-established water cycle. The dust distribution is identical in both simulations. The evolution of total ozone for the SPICAM ozone reanalysis, covering MY 27 and $L_S = 0$–68° of MY 28 (where SPICAM retrievals are still available), and the departure from the control simulation (SPICAM ozone reanalysis - control percentage difference) are displayed in Fig. 3a,b respectively. Values are given at local noon everywhere to provide an optimal average comparison to SPICAM total ozone retrievals (Fig. 2a), since just over 50% of the SPICAM total ozone retrievals are two hours either side of local noon. The general temporal and spatial distribution of ozone is as previously described by Lefèvre et al. (2004) and Lefèvre et al. (2008), with winter polar maximums and the least abundance in the southern hemisphere around perihelion.

The total ozone difference between the SPICAM ozone reanalysis and control simulation (Fig. 3b) indicates that in the equatorial regions the MGCM reproduces the total ozone abundance in the SPICAM retrievals effectively during the perihelion season, although there is a 25–30% increase in total ozone abundance at the start of the aphelion season (L_S =30–45°) from 30°S–30°N. In this spatio-temporal region, disagreement was also found between LMD GCM simulated total ozone and SPICAM retrievals by Clancy et al. (2016), although the largest difference was found slightly later in the aphelion season where no SPICAM retrievals for this particular Mars year are available at equatorial latitudes (L_S = 75–90° in Fig. 3b). Total ozone abundance poleward of 30°N from L_S =90–135° during northern summer displays a close match in the SPICAM ozone reanalysis and control simulation. During the equivalent season in the southern hemisphere (poleward latitudes of 30°S from L_S =250–315°), the MGCM tends to underestimate total ozone abundance, although total ozone amounts during this time period are extremely low at southern polar latitudes (see Fig. 3a).

Spatio-temporal regions displaying a large percentage disagreement (over 40%) in total ozone between the SPICAM ozone reanalysis and control simulation are found at latitudes between 45°S–10°S from L_S =135–180° and at northern polar (60°N–90°N) latitudes from L_S =150–195°, at the onset of northern polar winter. There is also an asymmetry in the total ozone difference at northern polar latitudes during periods of time around northern polar winter i.e. L_S =135–180° MY 27 and L_S =0–30° MY 28, with the control simulation underestimating total ozone by up to 40% from L_S = 135–180°, but generally by less than 20% from L_S = 0–30° in MY 28. The next sections explore potential causes for the total ozone differences identified in the SPICAM ozone reanalysis.

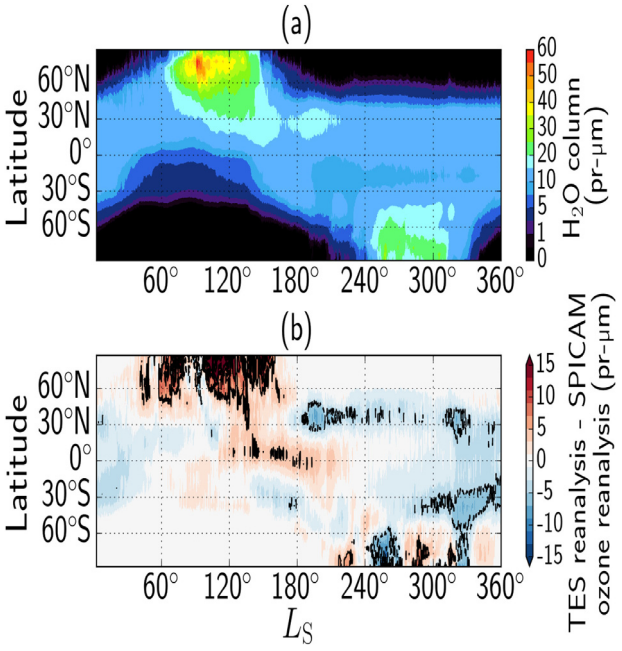

Fig. 4. (a) Zonally-averaged water vapour column in the SPICAM ozone reanalysis and (b) the difference in water vapour column between the TES water vapour reanalysis and the SPICAM ozone reanalysis. The solid/dashed contours mark a 5,10 and 15 pr-μm increase/decrease in the TES water vapour reanalysis.

4.1. Investigating global links between water vapour and ozone

The MGCM uses the recent microphysical scheme by Navarro et al. (2014b) which accounts for sublimation, condensation,sedimentation and nucleation of water ice particles in the atmosphere, includes supersaturation effects and also accounts for the effects of radiatively active water ice clouds. The primary destruction mechanism of ozone is chemical reactions with HO_x species, which are indirectly (but strongly) related to water vapour. Therefore, modelling errors in the water vapour distribution can also lead to a lack or overestimation of total ozone throughout a Mars year, affecting the global total ozone budget.

To determine whether the primary regions of large total ozone difference identified by the SPICAM ozone reanalysis (Fig. 3b) are due to an overestimation of water vapour column in the MGCM, the simulated water vapour column in the SPICAM ozone reanalysis is compared to a TES water vapour reanalysis using the method of Steele et al. (2014b). The year in which TES water vapour column retrievals are assimilated is different to the simulations (MY 26 compared to MY 27) but the yearly cycle is to a great degree repetitive (See Figure 12 of Wolkenberg et al., 2011), and so the broad seasonal/latitudinal differences are likely to be similar for any Mars year. The comparison of the simulated water vapour column in the MGCM and the TES water vapour reanalysis is an update of the comparison conducted by Steele et al. (2014b), with the MGCM used here including the updated microphysics package (Navarro et al., 2014b), the chemical species module (as a result water vapour is now treated as a chemically active species) and a correction to the vertical interpolation of tracer volume mixing ratio in the advection scheme that previously allowed for mass mixing ratios to increase to over 1 in particular regions where a chemical species is not vertically well mixed.

The simulated water vapour column in the SPICAM ozone reanalysis and deviations of the simulated water vapour column in the SPICAM ozone reanalysis from the TES water vapour reanalysis are displayed in Fig. 4a and 4 b respectively. A large dry bias of water vapour is present in Fig. 4 around peak northern summer sublimation from the northern polar cap (latitudes 70°N–90°N from L_S = 90–150°). This is less important with regards to total ozone since minimal ozone amounts are present in these locations. The dry bias in northern summer has been shown to be improved by including outlying deposits of water ice (Steele et al., 2014b).

At the start of the year and leading into the aphelion season (L_S = 0–60°) the SPICAM ozone reanalysis overpredicts the local water vapour column by up to 4 pr-μm at 30°S–45°N. There is also a wet bias in water vapour at 45°S–10°S from L_S =135–180° and during southern summer (L_S =245–270°) at latitudes southward of 60°S. All of the above identified wet biases correspond to regions in which total ozone is underestimated in the MGCM (see Fig. 3b).

A wet bias is also present from 30°N–60°N from L_S = 180° that continues through until the end of the year in Fig. 4b. During polar winter, a strong jet at around 65–75° latitude in both hemispheres provides a barrier to mixing between lower latitude chemical species and chemical species situated poleward of the jet. Fig. 3b hints at a slight underestimation of total ozone at these northern latitudes on the edge of availability of SPICAM retrievals from L_S = 270–330°. To determine if the continuing wet bias from 30°N–60°N throughout northern polar winter seen in Fig. 4b is likely to have an impact on the total ozone abundance in this region during northern polar winter, we can look at statistics from the assimilation process. The data assimilation process allows for tracking of the total ozone increments added in the SPICAM ozone reanalysis as the total ozone distribution evolves in space and time. Fig. 5 displays the total ozone increments as a result of the assimilation process during northern polar winter. Steele et al. (2014b) assimilated TES water vapour column and temperature profiles and investigated global transport of water vapour, indicating that for the time period covered in Fig. 5 the primary transport of water vapour northward of 45°N is by transient eddies and a wavenumber 2 stationary wave with increased transport to the west of Tharsis and over Arabia Terra. If the wet bias in water vapour from 30°N–60°N is causing the underestimation of total ozone in early spring seen in Fig. 3b, we would expect to see the SPICAM ozone reanalysis needing to increase total ozone west of the Tharsis region throughout northern winter. While this feature is not clearly seen before L_S =270° (Fig. 5a), an increase in total ozone is evident in Fig. 5b–d at high northern latitudes from 135W–180°W and at around 45°E i.e. west of Tharsis and over Arabia Terra.

The magnitude of the total ozone increment is at its maximum towards the end of northern polar winter, where total ozone increments exceed 0.2 μm-atm. Longitudinal variations in the total ozone increment are also evident. Holmes et al. (2017) indicate how northern polar total ozone is highly correlated to potential vorticity during northern polar winter, with the spatial distribution of total ozone being a good tracker for the polar vortex edge. The variation in positive and negative total ozone increments for the SPICAM ozone reanalysis in Fig. 5 across longitudinal space suggest that the polar vortex edge is likely to be misaligned. Further evidence is also displayed in the positive/negative variations in total ozone percentage difference particularly evident at 0°–30°N from L_S = 300–360° in Fig. 3b.

In conclusion, water vapour column biases in the MGCM can potentially account for underestimation of total ozone at the start of the aphelion season and at 45°S–10°S from L_S =135–180°. There are however regions in which the underestimation cannot be explained by water vapour column biases, such as at northern polar (60°N–90°N) latitudes from L_S =150–195°, where the MGCM underestimates the water vapour column found in the TES water vapour reanalysis. A wet water vapour bias is also evident at southern equatorial latitudes (0°–30°S) during the perihelion season but the total ozone in the SPICAM ozone reanalysis is in good agreement with the MGCM as shown in Fig. 3b, suggesting the vertical profiles of both water vapour and ozone are also key to

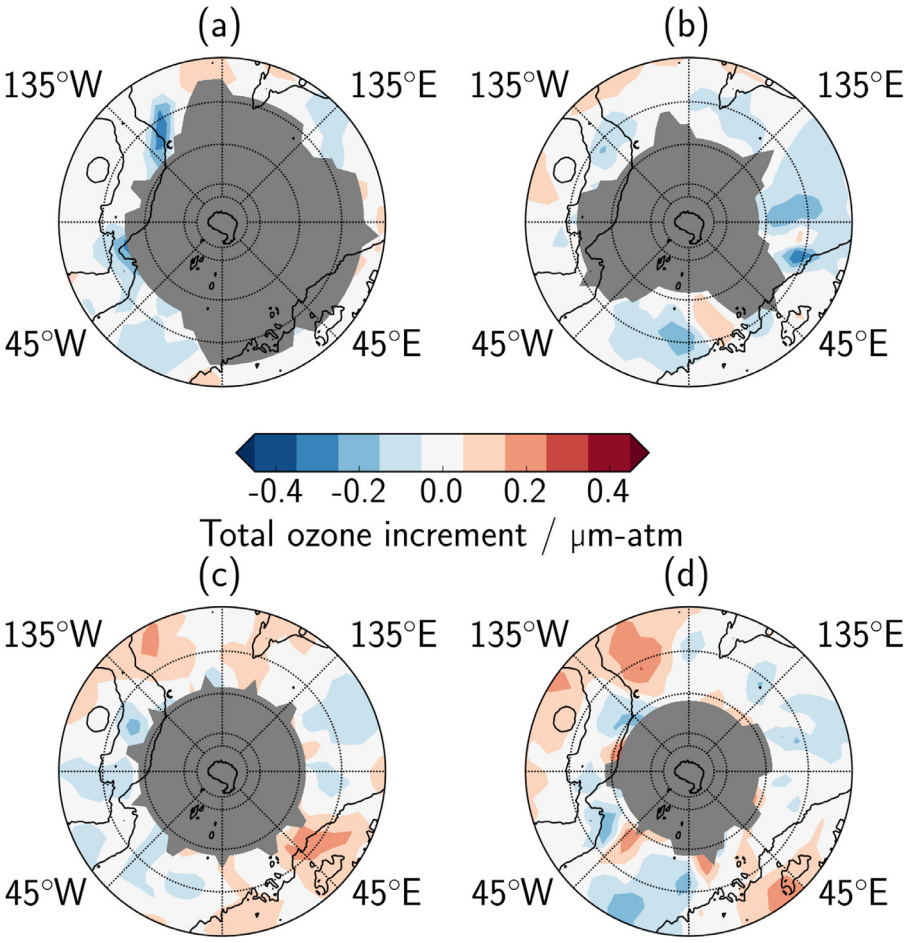

Fig. 5. Northern polar stereographic projections of the total ozone increments added in the SPICAM ozone reanalysis over the 30 sol period preceding a) L_S =270°, b) L_S =290°, c) L_S =310° and d) L_S =325° MY 27. Black contours indicate topography, and the gray shading indicates no direct increments added as a result of no nearby SPICAM retrievals at the time.

investigate. Assimilation of water vapour and ozone profiles, which will be retrieved from the NOMAD instrument on the ExoMars TGO spacecraft (Neefs et al., 2015; Patel et al., 2017) will be of great importance to determine the precise link between water vapour and ozone.

4.2. Water ice clouds and heterogeneous processes

With heterogeneous processes on water ice clouds (Lefèvre et al., 2008) active in both simulations, the distribution of water ice clouds is important for quantifying the local total ozone abundance. Fig. 6a and 6b display the water ice optical depth at 825 cm^{-1} from TES water ice optical depth retrievals and the SPICAM ozone reanalysis respectively (the control simulation displays minimal variation in water ice optical depth with the SPICAM ozone reanalysis). A similar comparison was performed in Steele et al. (2014b) albeit for a different Mars year and with an older microphysics package (Montmessin et al., 2004).

The seasonal cycle of water ice clouds in the equatorial region of the SPICAM ozone reanalysis (Fig. 6b) displays a reasonable agreement with the TES water ice optical depth retrievals in Fig. 6a, although the peak optical depth in the aphelion cloud belt is underestimated by around 25%. Optically thicker clouds are present in the polar hoods as a result of the low atmospheric temperatures, with TES water ice optical depth retrievals indicating higher values on the polar edge around northern and southern winter. Underestimation of the water ice optical depth in the MGCM could potentially account for underestimation of total ozone at the start of the aphelion season in Fig. 3b. The water ice optical depth at latitudes of 45°S–10°S from L_S =135–180° are well matched in the SPICAM ozone reanalysis and TES retrievals, suggesting this particular total ozone difference identified in Fig. 3b cannot be explained by modelling errors in water ice optical depth.

Water ice clouds on Mars are notoriously difficult to simulate accurately, in particular the opacity of the clouds are generally too high in most GCMs in the polar hoods (Haberle et al., 2011; Clancy et al., 2016). This is clearly true for the MGCM used in this investigation, with the water ice optical depth overestimated during polar winter in both hemispheres, comparing water ice optical depths at 30°N–45°N from L_S =240–360° in Fig. 6a and 6b for instance. While observations are available of water ice clouds inside the polar night from the MCS instrument (Benson et al., 2011), the actual thickness of water ice clouds in the polar hoods is uncertain since MCS cannot observe from the surface to an altitude of 10 km, precisely where GCMs predict the vertical extent of the entire cloud structure (Montmessin et al., 2004). Thicker simulated water ice clouds in the polar hood could potentially explain the difference in total ozone budget at northern polar (60°N–90°N) latitudes from L_S =150–195° in Fig. 3b, but as shown in Fig. 6 the MGCM already overestimates the water ice optical depth in this spatio-temporal region. If no increased heterogeneous uptake of HO_x species on water ice clouds does in fact occur, it is difficult to explain this one outstanding area in which the total ozone difference in the SPICAM ozone reanalysis and the control simulation differ, since it

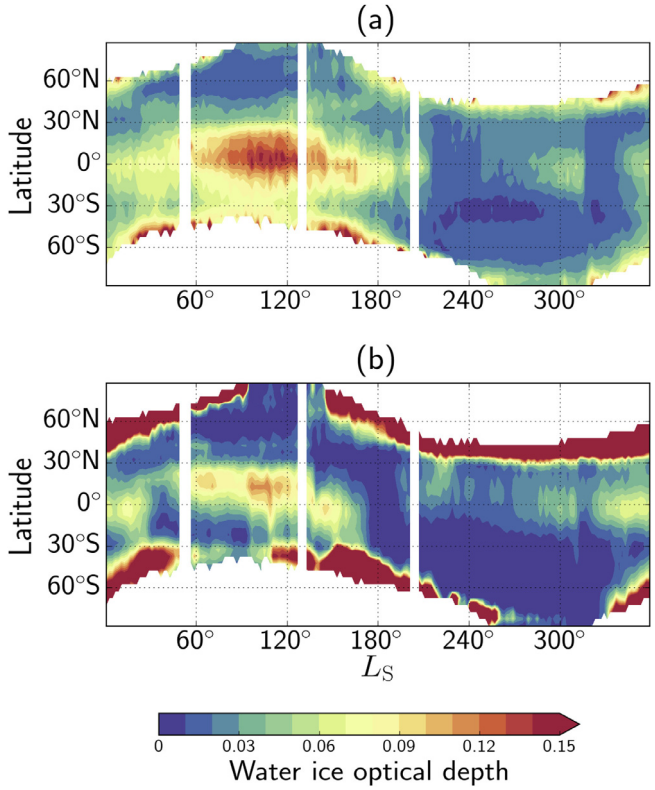

Fig. 6. (a) TES water ice optical depth retrievals at 825 cm^{-1} in MY 26 and (b) simulated zonally-averaged water ice optical depth at 825 cm^{-1} in the SPICAM ozone reanalysis at 2 p.m. local time covering MY 27. A mask has been applied to the model results to make the comparison clearer.

cannot be explained by model biases in water ice optical depth or water vapour column. Clancy et al. (2016) also found little correlation between water ice optical depth and total ozone in MARCI retrievals, providing further evidence that heterogeneous processes are unlikely to be the cause of the total ozone differences between the SPICAM ozone reanalysis and the control simulation. One potential explanation could be modelling errors in the simulated water vapour/ice and ozone vertical profiles, however this is outside the scope of the current investigation and will be investigated in the future using retrievals from the NOMAD instrument on the ExoMars TGO spacecraft (Neefs et al., 2015; Patel et al., 2017).

4.3. Total ozone during polar night

During polar night, the primary loss mechanisms for ozone are negligible, as photolysis cannot occur and the cold temperatures result in minimal water vapour concentration and hence a minimal presence of odd hydrogen species. Differences between the SPICAM ozone reanalysis and control simulation inside the polar night regions displayed in Fig. 3b (L_S = 100–120° at latitudes poleward of 75°S for example), where there are no retrievals from SPICAM nearby, result from the assimilation of retrievals in different spatio-temporal regions which are consequently evolved in time by the MGCM. Since ozone is quasi-passive in this spatio-temporal region (Lefèvre et al., 2004; Holmes et al., 2017), this emphasises how small deviations in the evolving annual ozone cycle can perpetuate to alter the distribution of total ozone in polar winter. The actual total ozone difference between the SPICAM ozone reanalysis and control simulation is generally small (at most times less than 2 μm-atm) compared to the amount of ozone present in the column (Fig. 3a). Since the ozone simulated in the SPICAM ozone reanalysis is part of an active chemical cycle, alterations to the total ozone will also lead to alterations in other chemical species such as O and O_2. Alterations in these chemical species will in turn lead to minor alterations in the simulated water vapour/ice cycle and hence potentially local alteration in dynamics through the radiative effect of water ice clouds. The total ozone difference during northern polar winter in the SPICAM ozone reanalysis and control simulation are as a result of slight alterations in the local dynamics, the causes of which will be the subject of a future paper.

The zonally-averaged vertical distribution of ozone for the control simulation and the SPICAM ozone reanalysis, averaged over L_S = 115–130°, is shown in Fig. 7a and 7b respectively. Although no nearby SPICAM retrievals have been assimilated into the MGCM for a long period of time in the southern polar region of the SPICAM ozone reanalysis at latitudes poleward of 75°S, the vertical distribution of ozone is different in the SPICAM ozone reanalysis (Fig. 7b) when compared to the control simulation (Fig. 7a). Whilst the near surface polar ozone layer is the same in both simulations, the high altitude ozone layer centred around 1 Pa (or roughly 65 km) is increased in abundance in the SPICAM ozone reanalysis.

This high altitude ozone layer has previously been investigated by Montmessin and Lefèvre (2013) and found to result from large-scale transport of oxygen-rich air from sunlit latitudes, balanced by the destruction of ozone through hydrogen radicals. The increased abundance of the high altitude ozone layer over the southern pole in the SPICAM ozone reanalysis is a result of alterations in the chemical state of the atmosphere, with the SPICAM ozone reanalysis continuing to increase total ozone abundance at equatorial latitudes from L_S = 90–120° by just below 10% in Fig. 3b.

Fig. 8a and 8b display the zonally-averaged vertical distribution of O and H for the SPICAM ozone reanalysis respectively, averaged over L_S = 115–130°. We hypothesise that the increased ozone in the SPICAM ozone reanalysis at equatorial latitudes from L_S = 90–120° and also slight alterations in water vapour results in the increased transport of oxygen-rich air, shown in Fig. 8c with an increase of O greater than 70% from 10–1 Pa. This is also coupled with a slight decrease in the transport of odd-hydrogen radicals to the southern polar region by around 20% centred on 1 Pa in Fig. 8d. The identified differences in the spatial distribution of southern polar winter total ozone for the SPICAM ozone reanalysis and control simulation demonstrate how data assimilation can be an effective tool for providing insight into regions where observational data is sparse or impossible, although observational data is clearly preferable.

5. Conclusions

We have assimilated, for the first time, total ozone into the MGCM to study the ozone cycle. Differences in the modelled and observed ozone cycle are efficiently identified by the assimilation process, with the largest total ozone percentage differences identified between 45°S–10°S from L_S =135–180° and at northern polar (60°N–90°N) latitudes from L_S =150–195°, at the onset of northern polar winter. An asymmetry in the magnitude of total ozone percentage differences in northern fall (L_S = 150–195°) and early northern spring (L_S = 0–30°) at northern polar latitudes is also identified.

Underestimated amounts of total ozone in the control simulation were found to be due to excessive northward transport of water vapour west of the Tharsis region and over Arabia Terra throughout northern polar winter resulting in increased increments in total ozone necessary in the SPICAM ozone reanalysis. Neither modelling biases in water vapour or heterogeneous processes on water ice clouds can explain outstanding differences in total ozone between the SPICAM ozone reanalysis and the control simulation at northern polar latitudes from L_S =150–195°. In this region in particular, investigation of the vertical profiles of water

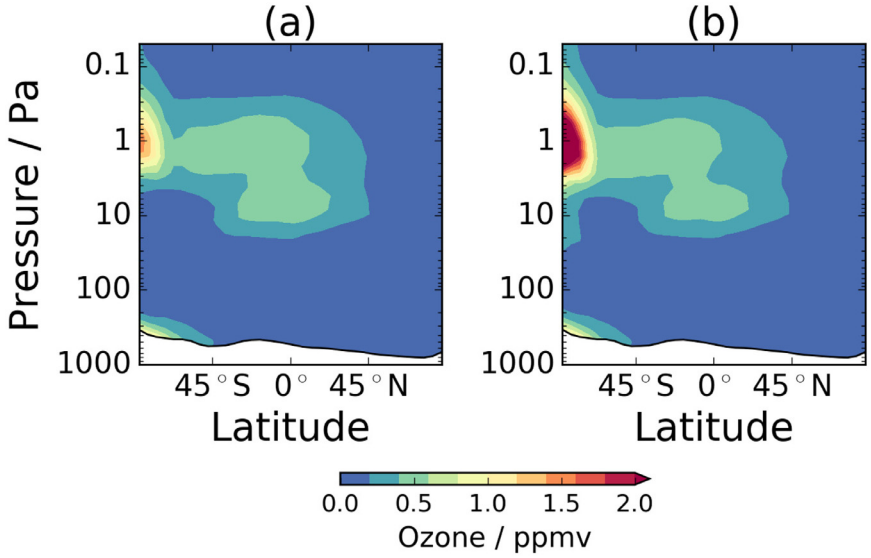

Fig. 7. Zonally-averaged vertical distribution of ozone for the (a) control simulation and (b) the SPICAM ozone reanalysis, averaged over L_S = 115–130°. The black contour line indicates the surface.

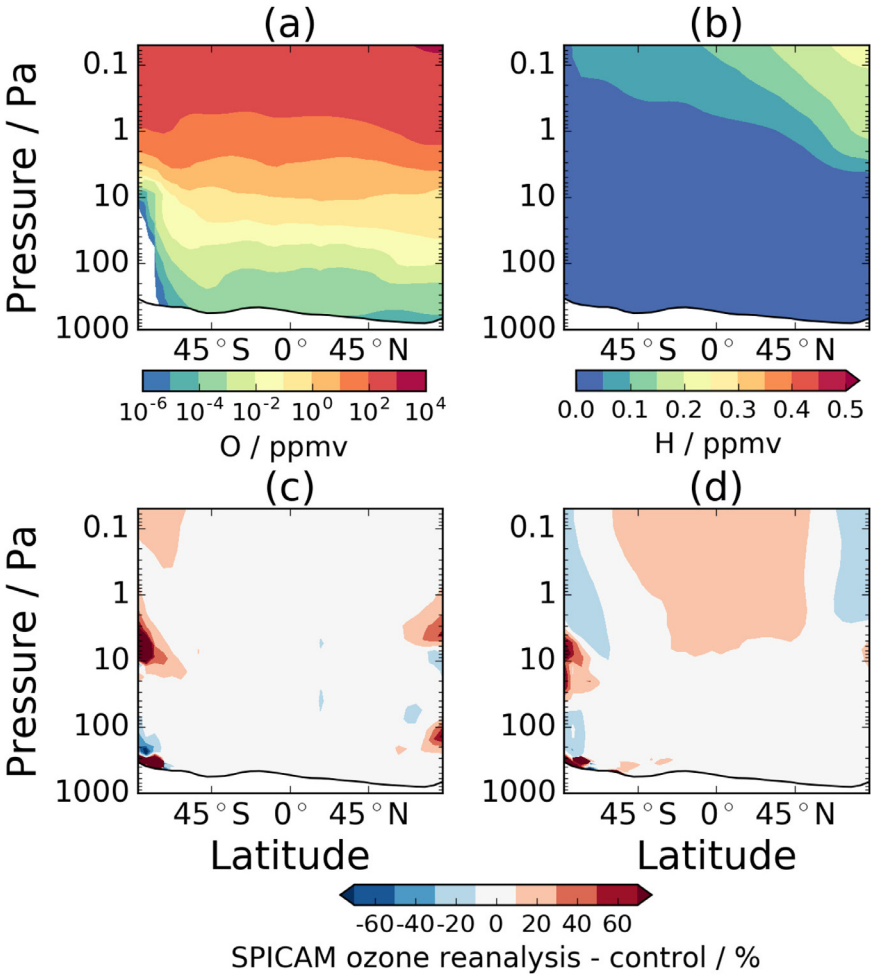

Fig. 8. Zonally-averaged vertical distribution of (a) O and (b) H for the SPICAM ozone reanalysis, averaged over L_S = 115–130°. The (SPICAM ozone reanalysis - control) percentage difference over the same time period is also displayed for (c) O and (d) H. The black contour line indicates the surface.

vapour/ice and ozone are needed to try and explain the difference in total ozone between the control simulation and SPICAM ozone reanalysis, and determine whether it is a further unidentified process which is not adequately represented.

The assimilation of SPICAM retrievals can also provide potential information on the polar maximum, with chemical changes as a result of the assimilation process affecting the southern polar high altitude ozone layer. For a more realistic study of the polar dynamics, assimilation of total ozone, and ideally water vapour too, would provide a more accurate ozone spatial distribution.

The lifetime of ozone in the atmosphere at different latitudes and times of the year presents an interesting problem for assimilation schemes. Under sunlit conditions, ozone can rapidly change in the space of 30 minutes. In the winter polar regions, ozone is quasi-passive and has a long lifetime. Chemical assimilation studies also help to inform future instrumentation planning to measure chemical species. Under sunlit conditions, rapid variations due to the insolation would require regular observations across several times of day for a better comparison to the modelled total ozone diurnal cycle. Data from instruments such as MARCI on the MRO spacecraft and the Imaging Ultraviolet Spectrograph on the Mars Atmosphere and Volatile Evolution spacecraft (Lefèvre et al., 2017), and in future from NOMAD on the ExoMars TGO spacecraft, will provide a more comprehensive dataset to assimilate, with the SPICAM observational dataset extremely useful also for cross-validation purposes. Assimilation of vertical profiles of ozone and water vapour/ice alongside column retrievals, such as will be possible from the NOMAD instrument on the ExoMars TGO, will also be of great use to further study the origin of differences in total ozone between the SPICAM ozone reanalysis and global circulation models.

Acknowledgments

The authors gratefully acknowledge the support of the UK Space Agency/STFC. JAH and SRL thank UKSA for support under grant ST/I003096/1, SRL also thanks STFC grant ST/L000776/1 and MRP thanks UKSA for support under grant ST/I003061/1 and ST/P001262/1. All authors acknowledge support as part of the project UPWARDS-633127, funded by the European Union Horizon 2020 Programme. We are grateful for an ongoing collaboration with François Forget and coworkers at LMD.

Supplementary material

Supplementary material associated with this article can be found, in the online version, at 10.1016/j.icarus.2017.11.026.

References

Altieri, F., Zasova, L., D'Aversa, E., Bellucci, G., Carrozzo, F.G., Gondet, B., Bibring, J.-P., 2009. O_2 1.27 μm emission maps as derived from OMEGA/MEx data. Icarus 204, 499–511.

Barth, C.A., Hord, C.W., Stewart, A.I., Lane, A.L., Dick, M.L., Anderson, G.P., 1973. Mariner 9 ultraviolet spectrometer experiment: seasonal variation of ozone on Mars. Science 179, 795–796.

Benson, J.L., Kass, D.M., Kleinböhl, A., 2011. Mars' north polar hood as observed by the Mars Climate Sounder. J. Geophys. Res. (Planets) 116, 3008.

Clancy, R.T., Nair, H., 1996. Annual (perihelion-aphelion) cycles in the photochemical behavior of the global Mars atmosphere. J. Geophys. Res. 101, 12785–12790.

Clancy, R.T., Sandor, B.J., García-Muñoz, A., Lefèvre, F., Smith, M.D., Wolff, M.J., Montmessin, F., Murchie, S.L., Nair, H., 2013. First detection of Mars atmospheric hydroxyl: CRISM near-IR measurement versus LMD GCM simulation of OH Meinel band emission in the Mars polar winter atmosphere. Icarus 226, 272–281.

Clancy, R.T., Wolff, M.J., Lefèvre, F., Cantor, B.A., Malin, M.C., Smith, M.D., 2016. Daily global mapping of Mars ozone column abundances with MARCI UV band imaging. Icarus 266, 112–133. doi:10.1016/j.icarus.2015.11.016.

Colaïtis, A., Spiga, A., Hourdin, F., Rio, C., Forget, F., Millour, E., 2013. A thermal plume model for the Martian convective boundary layer. J. Geophys. Res. (Planets) 118, 1468–1487. doi:10.1002/jgre.20104.

Conrath, B.J., Pearl, J.C., Smith, M.D., Maguire, W.C., Christensen, P.R., Dason, S., Kaelberer, M.S., 2000. Mars Global Surveyor Thermal Emission Spectrometer (TES) observations: atmospheric temperatures during aerobraking and science phasing. J. Geophys. Res. 105, 9509–9520. doi:10.1029/1999JE001095.

Eskes, H.J., van Velthoven, P.F.J., Valks, P.J.M., Kelder, H.M., 2003. Assimilation of GOME total ozone satellite observations in a three-dimensional tracer transport model. Q. J. R. Meteorol. Soc. 129, 1663–1681.

Fast, K., Kostiuk, T., Espenak, F., Annen, J., Buhl, D., Hewagama, T., A'Hearn, M.F., Zipoy, D., Livengood, T.A., Sonnabend, G., Schmülling, F., 2006. Ozone abundance on Mars from infrared heterodyne spectra. I. Acquisition, retrieval, and anticorrelation with water vapor. Icarus 181, 419–431.

Fedorova, A., Korablev, O., Perrier, S., Bertaux, J.-L., Lefevre, F., Rodin, A., 2006. Observation of o_2 1.27 μm dayglow by SPICAM IR: seasonal distribution for the first Martian year of Mars express. J. Geophys. Res. (Planets) 111, E09S07. doi:10.1029/2006JE002694.

Forget, F., Hourdin, F., Fournier, R., Hourdin, C., Talagrand, O., Collins, M., Lewis, S.R., Read, P.L., Huot, J.-P., 1999. Improved general circulation models of the Martian atmosphere from the surface to above 80 km. J. Geophys. Res. 104, 24155–24176.

Grassi, B., Redaelli, G., Visconti, G., 2004. Assimilation of stratospheric ozone in the chemical transport model STRATAQ. Ann. Geophys. 22, 2669–2678.

Greybush, S.J., Wilson, R.J., Hoffman, R.N., Hoffman, M.J., Miyoshi, T., Ide, K., McConnochie, T., Kalnay, E., 2012. Ensemble Kalman filter data assimilation of Thermal Emission Spectrometer temperature retrievals into a Mars GCM. J. Geophys. Res. 117, 11008.

Haberle, R.M., Wolff, M.J., Hollingsworth, J., Kahre, M.A., 2011. Comparing MARCI cloud observations with the NASA/Ames Mars General Circulation Model. AGU Fall Meeting Abstracts A1654.

Hoffman, M.J., Eluszkiewicz, J., Weisenstein, D., Uymin, G., Moncet, J.-L., 2012. Assessment of Mars atmospheric temperature retrievals from the Thermal Emission Spectrometer radiances. Icarus 220, 1031–1039.

Holmes, J.A., 2015. Atmospheric modelling and data assimilation of trace gases on Mars. Ph.D. thesis. The Open University.

Holmes, J.A., Lewis, S.R., Patel, M.R., 2017. On the link between Martian total ozone and potential vorticity. Icarus 282, 104–117. doi:10.1016/j.icarus.2016.10.004.

Kiesewetter, G., Sinnhuber, B.-M., Vountas, M., Weber, M., Burrows, J.P., 2010. A long-term stratospheric ozone data set from assimilation of satellite observations: high-latitude ozone anomalies. J. Geophys. Res. 115, 10307.

Krasnopolsky, V.A., 2006. Photochemistry of the martian atmosphere: seasonal, latitudinal, and diurnal variations. Icarus 185, 153–170.

Krasnopolsky, V.A., 2009. Seasonal variations of photochemical tracers at low and middle latitudes on Mars: observations and models. Icarus 201, 564–569.

Krasnopolsky, V.A., Parshev, V.A., 1979. Ozone and photochemistry of the Martian lower atmosphere. Planet. Space Sci. 27, 113–120.

Lahoz, W., Geer, A., Bannister, R., et al., 2005. Assimilation of Ozone and Water Vapour into the Unified Model (69). ESA Special Publication. Envisat ERS Symposium, 572.

Lefèvre, F., Bertaux, J.-L., Clancy, R.T., Encrenaz, T., Fast, K., Forget, F., Lebonnois, S., Montmessin, F., Perrier, S., 2008. Heterogeneous chemistry in the atmosphere of Mars. Nature 454, 971–975.

Lefèvre, F., Lebonnois, S., Montmessin, F., Forget, F., 2004. Three-dimensional modeling of ozone on Mars. J. Geophys. Res. 109, 7004.

Lefèvre, F., Montmessin, F., Schneider, N.M., Deighan, J., Jain, S.K., Stewart, A.I.F., Chaffin, M.S., Crismani, M., McClintock, W.E., Holsclaw, G.M., Jakosky, B.M., Stiepen, A., Lo, D.Y., Yelle, R., Clarke, J.T., 2017. Mars Ozone mapping with MAVEN IUVS. In: Forget, F., Millour, M. (Eds.), The Mars Atmosphere: Modelling and Observation, p. 4201.

Levelt, P.F., Allaart, M.A.F., Kelder, H.M., 1996. On the assimilation of total-ozone satellite data. Ann. Geophys. 14, 1111–1118.

Lewis, S.R., Barker, P.R., 2005. Atmospheric tides in a Mars general circulation model with data assimilation. Adv. Space Res. 36, 2162–2168.

Lewis, S.R., Read, P.L., Conrath, B.J., Pearl, J.C., Smith, M.D., 2007. Assimilation of thermal emission spectrometer atmospheric data during the Mars Global Surveyor aerobraking period. Icarus 192, 327–347.

Lorenc, A.C., Bell, R.S., MacPherson, B., 1991. The meteorological office analysis correction data assimilation scheme. Q. J. R. Meteorol. Soc. 117, 59–89.

Madeleine, J.-B., Forget, F., Millour, E., Montabone, L., Wolff, M.J., 2011. Revisiting the radiative impact of dust on Mars using the LMD Global Climate Model. J. Geophys. Res. (Planets) 116, E11010. doi:10.1029/2011JE003855.

Montabone, L., Forget, F., Millour, E., Wilson, R.J., Lewis, S.R., Cantor, B., Kass, D., Kleinböhl, A., Lemmon, M.T., Smith, M.D., Wolff, M.J., 2015. Eight-year climatology of dust optical depth on Mars. Icarus 251, 65–95. doi:10.1016/j.icarus.2014.12.034.

Montabone, L., Lewis, S.R., Read, P.L., Hinson, D.P., 2006. Validation of martian meteorological data assimilation for MGS/TES using radio occultation measurements. Icarus 185, 113–132.

Montmessin, F., Forget, F., Rannou, P., Cabane, M., Haberle, R.M., 2004. Origin and role of water ice clouds in the Martian water cycle as inferred from a general circulation model. J. Geophys. Res. (Planets) 109, 10004.

Montmessin, F., Lefèvre, F., 2013. Transport-driven formation of a polar ozone layer on Mars. Nat. Geosci. 6, 930–933. doi:10.1038/ngeo1957.

Moreau, D., Esposito, L.W., Brasseur, G., 1991. The chemical composition of the dust-free Martian atmosphere - preliminary results of a two-dimensional model. J. Geophys. Res. 96, 7933–7945.

Navarro, T., Forget, F., Millour, E., Greybush, S.J., 2014. Detection of detached dust layers in the Martian atmosphere from their thermal signature using assimilation. Geophys. Res. Lett. 41, 6620–6626. doi:10.1002/2014GL061377.

Navarro, T., Madeleine, J.-B., Forget, F., Spiga, A., Millour, E., Montmessin, F., Määttänen, A., 2014. Global climate modeling of the Martian water cycle with improved microphysics and radiatively active water ice clouds. J. Geophys. Res. (Planets) 119, 1479–1495. doi:10.1002/2013JE004550.

Neefs, E., Vandaele, A.C., Drummond, R., Thomas, I.R., Berkenbosch, S., Clairquin, R., Delanoye, S., Ristic, B., Maes, J., Bonnewijn, S., Pieck, G., Equeter, E., Depiesse, C., Daerden, F., Ransbeeck, E.V., Nevejans, D., Rodriguez-Gómez, J., López-Moreno, J.-J., Sanz, R., Morales, R., Candini, G.P., Pastor-Morales, M.C., Aparicio del Moral, B., Jeronimo-Zafra, J.-M., Gómez-López, J.M., Alonso-Rodrigo, G., Pérez-Grande, I., Cubas, J., Gomez-Sanjuan, A.M., Navarro-Medina, F., Thibert, T., Patel, M.R., Bellucci, G., De Vos, L., Lesschaeve, S., Vooren, N.V., Moelans, W., Aballea, L., Glorieux, S., Baeke, A., Kendall, D., De Neef, J., Soenen, A., Puech, P.-Y., Ward, J., Jamoye, J.-F., Diez, D., Vicario-Arroyo, A., Jankowski, M., 2015. NOMAD spectrometer on the ExoMars trace gas orbiter mission: part 1—design, manufacturing and testing of the infrared channels. Appl. Opt. 54, 8494–8520. doi:10.1364/AO.54.008494.

Newman, C.E., Lewis, S.R., Read, P.L., Forget, F., 2002. Modeling the Martian dust cycle, 1. Representations of dust transport processes. J. Geophys. Res. 107, 5123.

Patel, M.R., Antoine, P., Mason, J., Leese, M., Hathi, B., Stevens, A.H., Dawson, D., Gow, J., Ringrose, T., Holmes, J., Lewis, S.R., Beghuin, D., van Donink, P., Ligot, R., Dewandel, J.-L., Hu, D., Bates, D., Cole, R., Drummond, R., Thomas, I.R., Depiesse, C., Neefs, E., Equeter, E., Ristic, B., Berkenbosch, S., Bolsée, D., Willame, Y., Vandaele, A.C., Lesschaeve, S., Vos, L.D., Vooren, N.V., Thibert, T., Mazy, E., Rodriguez-Gomez, J., Morales, R., Candini, G.P., Pastor-Morales, M.C., Sanz, R., del Moral, B.A., Jeronimo-Zafra, J.-M., Gómez-López, J.M., Alonso-Rodrigo, G., Pérez-Grande, I., Cubas, J., Gomez-Sanjuan, A.M., Navarro-Medina, F., BenMoussa, A., Giordanengo, B., Gissot, S., Bellucci, G., Lopez-Moreno, J.J., 2017. NOMAD spectrometer on the exomars trace gas orbiter mission: part 2—design, manufacturing, and testing of the ultraviolet and visible channel. Appl. Opt. 56 (10), 2771–2782. doi:10.1364/AO.56.002771.

Perrier, S., Bertaux, J.L., Lefèvre, F., Lebonnois, S., Korablev, O., Fedorova, A., Montmessin, F., 2006. Global distribution of total ozone on Mars from SPICAM/MEX UV measurements. J. Geophys. Res. 111, E09S06.

Spiga, A., Forget, F., 2009. A new model to simulate the Martian mesoscale and microscale atmospheric circulation: validation and first results. J. Geophys. Res. 114, E02009.

Steele, L.J., Lewis, S.R., Patel, M.R., 2014. The radiative impact of water ice clouds from a reanalysis of Mars Climate Sounder data. Geophys. Res. Lett. 41, 4471–4478.

Steele, L.J., Lewis, S.R., Patel, M.R., Montmessin, F., Forget, F., Smith, M.D., 2014. The seasonal cycle of water vapour on Mars from assimilation of Thermal Emission Spectrometer data. Icarus 237, 97–115.

Wolkenberg, P., Smith, M.D., Formisano, V., Sindoni, G., 2011. Comparison of PFS and TES observations of temperature and water vapor in the martian atmosphere. Icarus 215, 628–638.